A 2D description of the single crystal thin plate growth from the melt by micro- pulling- down method. Part 2

Agneta M. BALINT[1], Stefan BALINT*,[2]

*Corresponding author
[1]Department of Physics, West University of Timisoara,
Blvd. V. Parvan 4, 300223 Timisoara, Romania,
balint@physics.uvt.ro
[2]Department of Computer Science, West University of Timisoara,
Blvd. V. Parvan 4, 300223 Timisoara, Romania,
stefan.balint@e-uvt.ro*

DOI: 10.13111/2066-8201.2018.10.3.5

Received: 31 May 2018/ Accepted: 30 June 2018/ Published: September 2018

Abstract: *This paper is the second part of a 2D description of a single crystal thin plate growth by micro-pulling–down (μ-PD) method. This part concerns the following aspects: temperature distribution and melt flow in the melt–crystal system (section 2); impurity distribution (section 3). Numerical illustration concerning the above aspects are given for the growth of a thin Si plate of 0.0001 [m] by using COMSOL Multiphysics software. The advantage of this description is that it helps in the better understanding of the impurity dispersion in meniscus and may help the improvement of crystal quality.*

Key Words: *modelling, thin plate growth from the melt, micro-pulling-down method*

1. INTRODUCTION

The 2-D geometry of a static stable Si meniscus, whose meridian curve was determined in the paper [1], and a Si tape of $0.0001[m]$ half thickness and of $0.0006[m]$ length, are represented in Fig. 1.

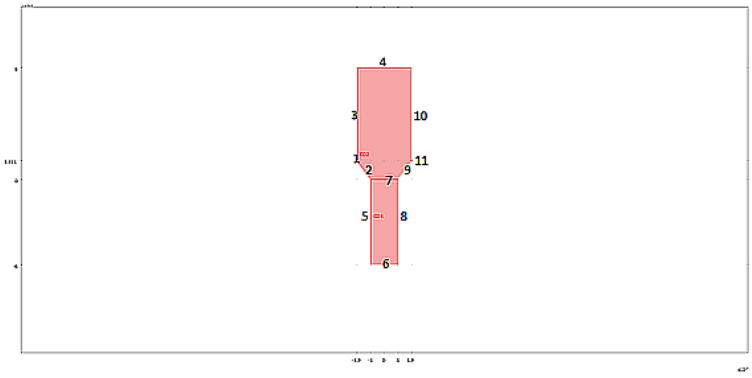

Figure 1. The 2-D geometry in which the temperature distribution, the melt flow and the impurity dispersion are computed

2. TEMPERATURE DISTRIBUTION AND MELT FLOW IN THE CRYSTAL- MELT SYSTEM IN A PD GROWTH PROCESS

Investigation of the temperature distribution in the crystal – melt system requires simultaneous consideration of the heat flows in the crystal-melt system (which is a Stefan problem with moving boundary where a heat source is located at the crystallization front) and the Navier-Stokes equation for the flows associated with both melt crystallization and convection. The equations, which govern the flow in the above 2D domain, are the incompressible Navier-Stokes equations:

$$\begin{cases} \rho\dfrac{\partial \vec{u}}{\partial t} + \rho(\vec{u}\cdot\nabla)\vec{u} = -\nabla p + \eta\Delta\vec{u} + \vec{F} \\ \nabla\vec{u} = 0 \end{cases} \tag{1}$$

In equations (1):

- in the sub-domain CO2, according to [2], $\rho(T) = 2580 - 1.59\cdot 10^{-1}\cdot(T - T_m) - 1.15\cdot 10^{-4}\cdot(T - T_m)^2\,[kg/m^3]$ is the temperature-dependent melt density and $\rho_m = 2580[kg/m^3]$ is the melt density at melting temperature $T_m = 1687[K]$.
- in the sub-domain CO1, according to [3], $\rho = 2300[kg/m^3]$;
- in the sub-domain CO2, according to[2], $\eta(T) = 0.75\cdot 10^{-3} - 1.22\cdot 10^{-6}\cdot(T - T_m)[Pa]$ is the temperature-dependent melt viscosity and $\eta_m = 0.75\cdot 10^{-3}[Pa]$ is the melt viscosity at the melting temperature ; in the sub-domain CO1, according to [3], $\eta_m = 0.75\cdot 10^{-3}$[Ps];
- $\vec{u}$ is the flow velocity field in CO2; p is the dynamic pressure field in CO2;

$\vec{F} = \rho\cdot\vec{g}$ is the volume force field, which incorporates in domain CO2 also the buoyancy force field $\beta(T)\cdot\rho_m\cdot\vec{j}$;

- $\beta(T) = 6.18\cdot 10^{-5}\cdot(T - T_m) + 4.72\cdot 10^{-8}\cdot(T - T_m)^2$ is the temperature-dependent heat expansion coefficient in CO2;

In CO2 the flow is generated by $\vec{F}$, the outlet velocity $U = 0.0001[m/s]$ equal to the pulling rate applied at the boundary 6 and the Marangoni flow due to the surface tension variation on boundaries 2 and 9. According to [2], in this case the temperature-dependent surface tension is given by $\gamma(T) = 0.765 - 0.016\cdot 10^{-3}\cdot(T - T_m)[N/m]$ and $\gamma_m = 0.765[N/m]$ is the surface tension at melting temperature. Since region with high surface tension pulls more strongly on the surrounding liquid than that with a low surface tension, the presence of a gradient in surface tension will naturally cause the liquid to flow away from regions of low surface tension. The stress caused by the gradient of the surface tension acts tangentially to the gas-liquid interface and generates the liquid flow. The above liquid flow is referred to as thermal Marangoni flow (convection). This is a boundary condition that acts at the free surface of the fluid (typically a gas-liquid interface) modelled with the incompressible Navier-Stokes equations. Note that the surface tension gradient can also be caused by gradient of concentration and the resulting flow is called Marangoni flow. The velocity field $\vec{u}$ is subjected to the following boundary conditions:

- on the boundaries 1, 3, 10 and 11, $\vec{u}$ satisfies the no slip condition;
- on the boundary 4, $\vec{u}$ satisfies inlet condition;

- on the boundary 6, $\vec{u}$ satisfies outlet condition, i.e. $\vec{u}$ is equal to the vertical pulling rate, i.e. $\vec{u} = -0.0001\vec{j}[m/s]$;
- on the boundary 7, $\vec{u}$ satisfies the continuity condition;
- on the boundaries 5 and 8, $\vec{u}$ satisfies the slip condition;
- according to [4], on the boundaries 2 and 9 – due to the thermal Marangoni flow - $\vec{u}$ satisfies the equation

$$\eta \cdot \frac{\partial \vec{u}}{\partial \vec{n}}\bigg| = -\frac{d\gamma}{dT} \cdot \nabla T \tag{2}$$

where $\vec{n}$ is the outward normal to the meridian curve of meniscus.

The velocity field $\vec{u}$ is also subjected to the following initial condition: $\vec{u}(t_0) = 0$ and $p(t_0) = 0$. The heat transport equation in the considered 2D domain is that of the heat transport by convection and conduction:

$$\rho \cdot C_p \cdot \frac{\partial T}{\partial t} + \nabla\left(-\lambda \nabla T\right) = Q - \rho \cdot C_p \cdot \vec{u} \cdot \nabla T \tag{3}$$

In this equation: ρ is the temperature-dependent melt density and $\rho = 2300[kg/m^3]$ is the crystal density; $C_p = 950[J/kg \cdot K]$ is the heat capacity at constant pressure(the same in the melt and in the crystal); T is the unknown temperature; $\lambda = 60[W/(m \cdot K)]$ is the thermal conductivity in the melt and $\lambda = 20[W/(m \cdot K)]$ in the crystal; Q is a heat source due to the release of the latent heat $\Lambda = 1.81 \cdot 10^6 [J/kg]$ [2] in the neighbourhood of the crystallization front h, i.e. in the region where the temperature is within the limits $(1686, 1687)[K]$. The unknown temperature T is subjected to the following boundary conditions: on the boundaries 1, 3, 4, 10, 11, T is a constant equal to $1690[K]$; on the interior boundary 7, T satisfies the continuity condition; on boundaries 2 and 9, there is an outer heat flux equal to $4.9 \cdot 10^5 [W/m^2]$; on the boundaries 5, 6 and 8 there is an outer heat flux equal to $1 \cdot 10^5 [W/m^2]$. The temperature T is also subjected to the initial condition $T(t_0) = 1690[K]$. In Figs. 2-14, different details concerning the computed flow field, pressure field and thermal field in the melt and in the crystal are presented.

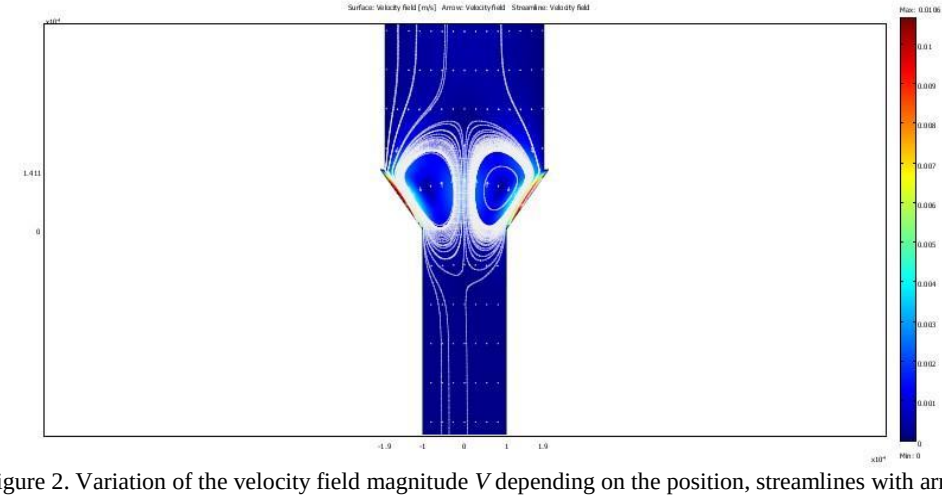

Figure 2. Variation of the velocity field magnitude V depending on the position, streamlines with arrows

According to Fig. 2, the velocity field magnitude varies depending on the position in the sample in the range $[0, 1.06 \cdot 10^{-2}][m/s]$. The streamline patterns in the meniscus show the effect of the Marangoni flows on the boundaries 2 and 9. On the boundary 2 the Marangoni flow is generated by the tangential stress $F_x = 1.6 \cdot 10^{-5} \cdot 0.580935 \left| -0.580935 T_x + 0.813949 T_y \right|$, $F_y = -1.6 \cdot 10^{-5} \cdot 0.813949 \left| -0.580935 T_x + 0.813949 T_y \right|$ and on the boundary 9 by the tangential stress $F_x = -1.6 \cdot 10^{-5} \cdot 0.580935 \left| 0.580935 T_x + 0.813949 T_y \right|$, $F_y = -1.6 \cdot 10^{-5} \cdot 0.813949 \left| 0.580935 T_x + 0.813949 T_y \right|$, respectively.

When these tangential stresses are equal to zero (slip condition), then the velocity field magnitude *V*, the streamlines with arrows look as in Fig. 3.

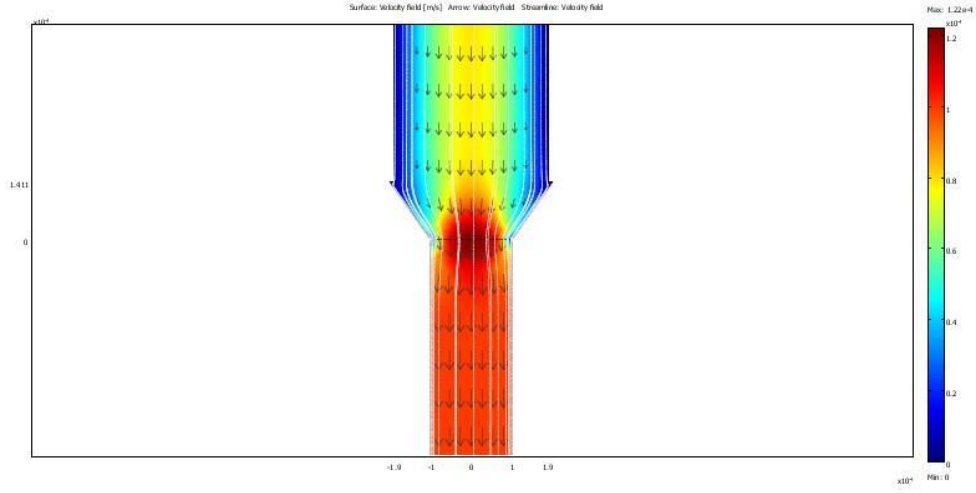

Figure 3. Variation of the velocity field magnitude *V* depending on the position for zero tangential stress

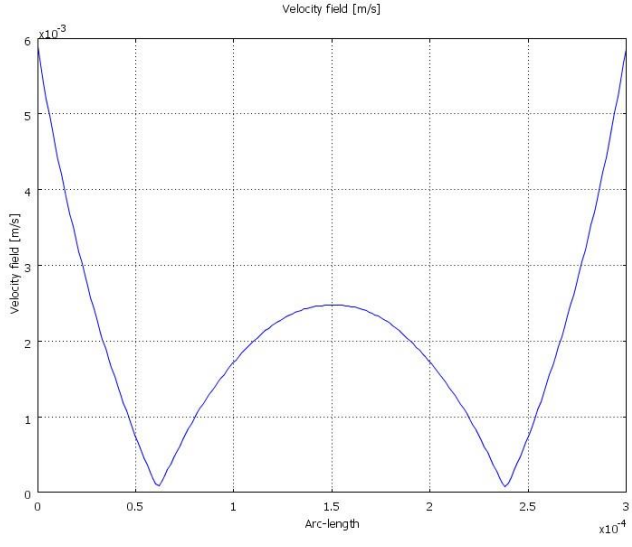

Figure 4. Variation of the velocity field magnitude *V* across the meniscus computed along the line defined by $y = 10^{-4}[m]$

According to Fig. 4, the variation of the velocity field magnitude *V* across the meniscus along the line $y = 10^{-4}[m]$ is in the range $[10^{-4}, 6 \cdot 10^{-3}][m/s]$.

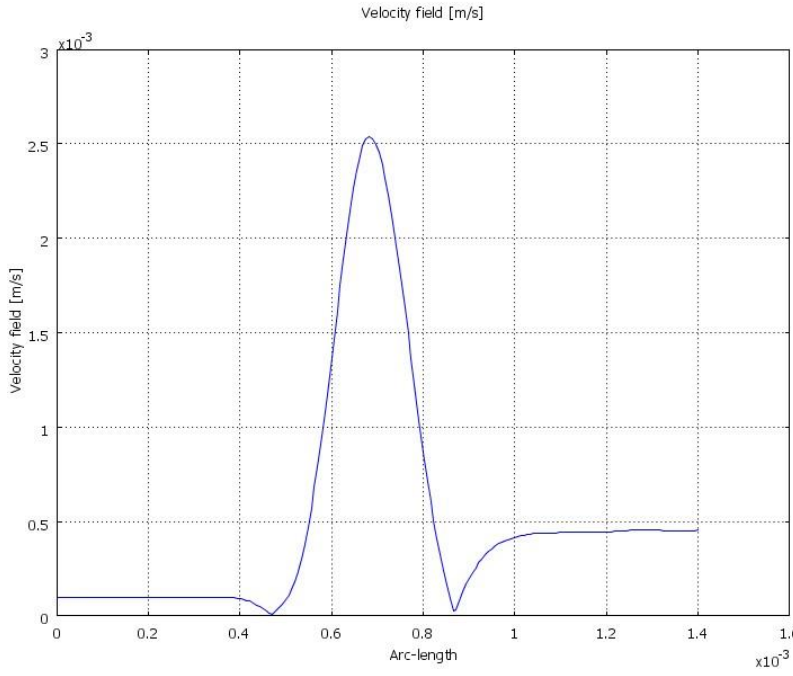

Figure 5. Variation of the velocity field magnitude *V* along the sample computed on the OY axis

According to Fig. 5, the variation of the velocity field magnitude *V* along the OY axis ranges between $\left[10^{-4}, 2.51 \cdot 10^{-3}\right][m/s]$.

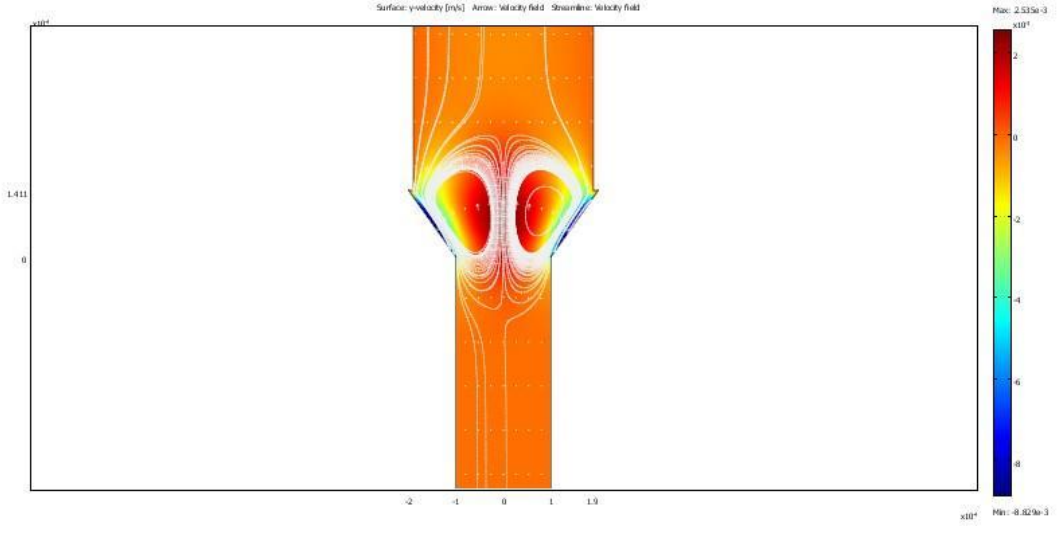

Figure 6. Variation of the v_y velocity field magnitude in the sample, streamlines with arrows

According to Fig. 6, the v_y velocity field magnitude varies, ranging between $\left[-8.829 \cdot 10^{-3}, 2.535 \cdot 10^{-3}\right][m/s]$.

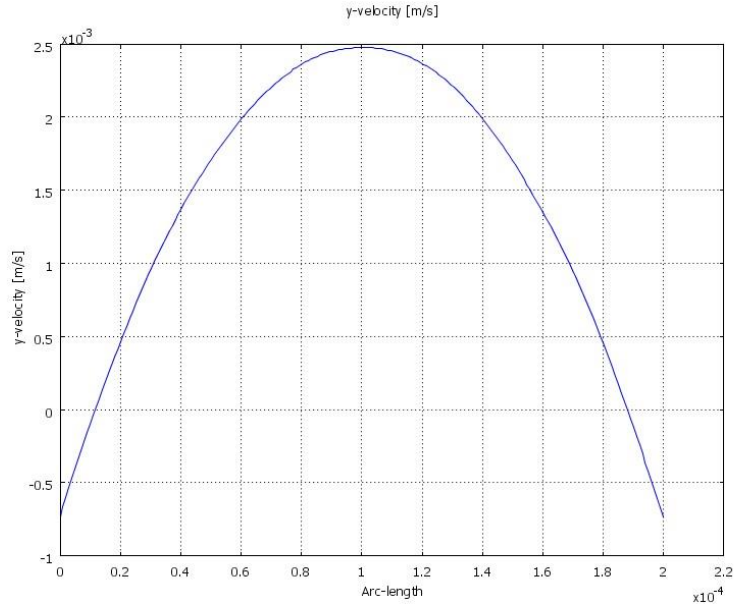

Figure 7. Variation of the v_y velocity field magnitude across the meniscus computed along the line defined by $y = 10^{-4}[m]$

According to Fig. 7, the variation of the v_y velocity field magnitude across the meniscus along the line $y = 10^{-4}[m]$ ranges between $\left[-0.75 \cdot 10^{-4}, 2.5 \cdot 10^{-3}\right][m/s]$.

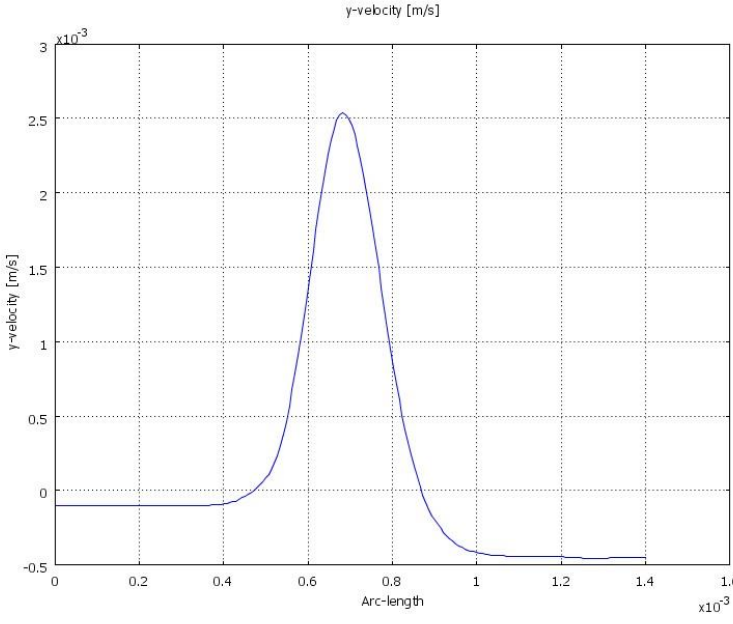

Figure 8. Variation of the v_y velocity field magnitude along the sample computed on the OY axis.

According to Fig. 8, the variation of the v_y velocity field magnitude along the OY axis ranges between $\left[-0.5 \cdot 10^{-3}, 2.5 \cdot 10^{-3}\right][m/s]$.

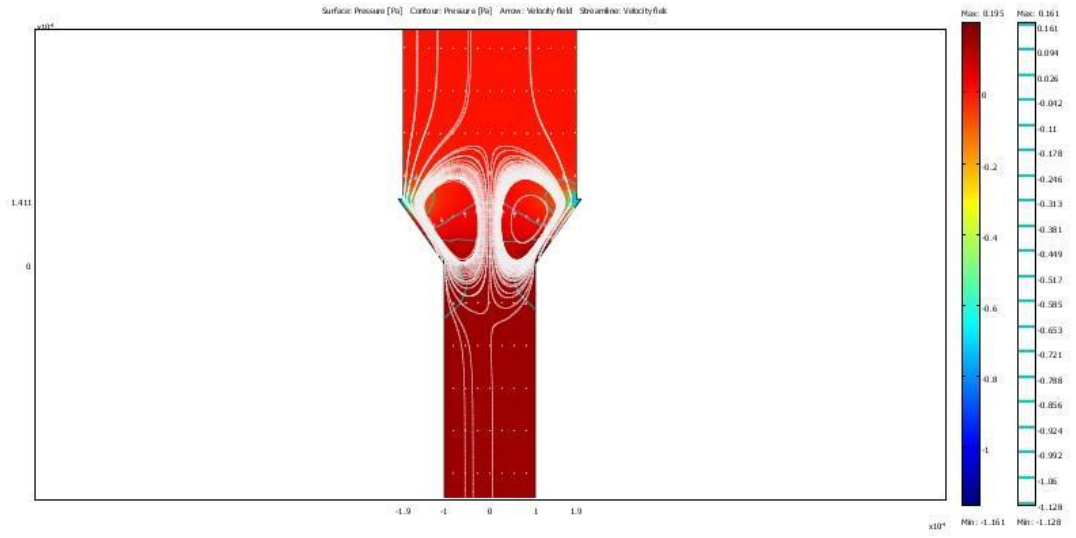

Figure 9. Dependence of the pressure field p on the position, isobars, streamlines with arrows

According to Fig. 9, the pressure field $p = p_m + p_M$ magnitude varies depending on the position ranging between $[-1.161, 0.195][Pa]$. Taking into account the value of $-p_g + \rho \cdot g \cdot h_m$, which is of order $-10^3[Pa]$, neglecting $p = p_m + p_M$ with respect to $-p_g + \rho \cdot g \cdot h_m$ is justified.

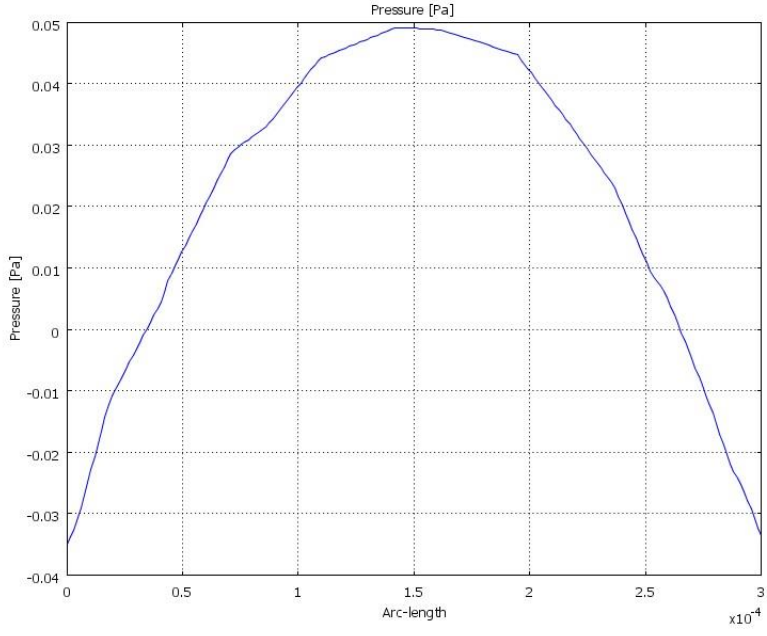

Figure 10. Variation of the pressure field magnitude $p = p_m + p_M$ across the meniscus, computed on the line defined by $y = 10^{-4}[m]$

According to Fig. 10, the variation of the pressure field $p = p_m + p_M$ magnitude across the meniscus computed along the line $y = 10^{-4}[m]$ ranges between $[-3.5 \cdot 10^{-2}, 5 \cdot 10^{-2}][Pa]$.

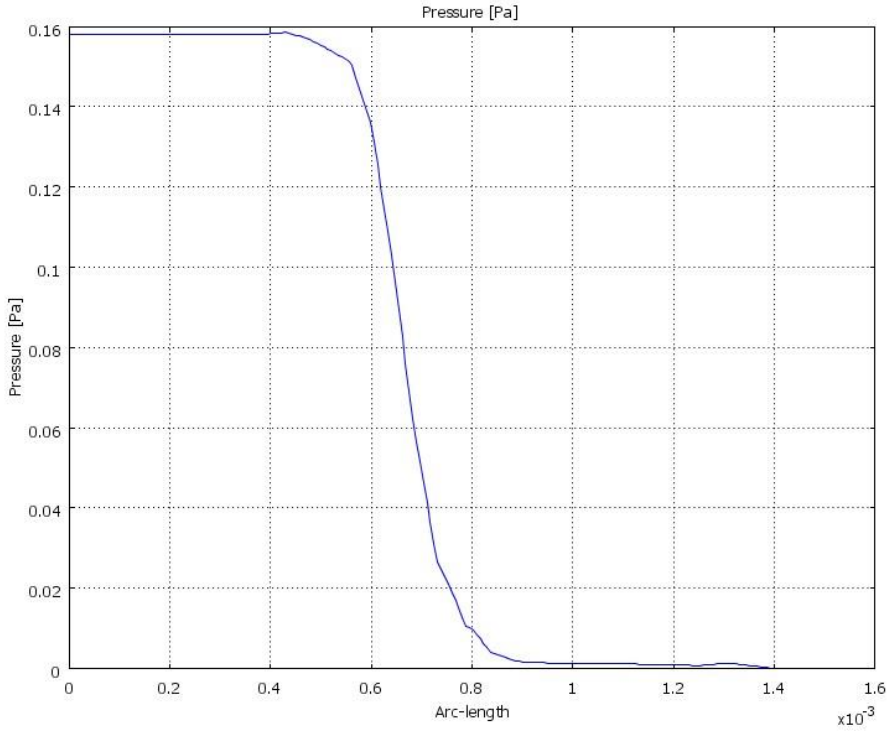

Figure 11. Variation of the pressure field $p = p_m + p_M$ magnitude along the sample, computed on the OY axis

According to Fig. 11, the variation of the pressure field $p = p_m + p_M$ along the OY axis is in the range of $[0, 1.6 \cdot 10^{-1}][Pa]$.

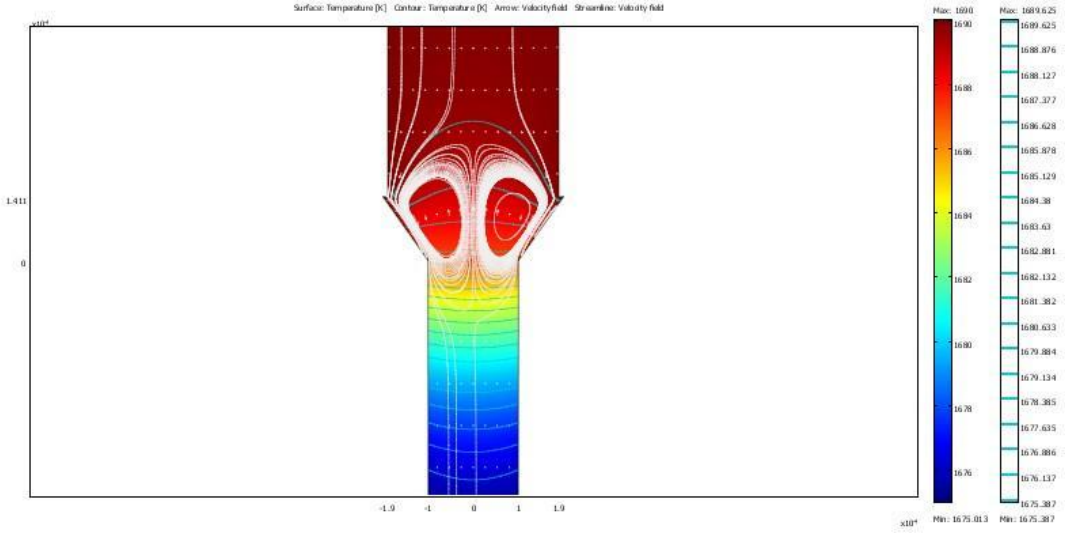

Figure 12. Dependence of the temperature field T on the position, isotherms, streamlines with arrows

According to Fig. 12, the temperature field magnitude varies depending on the position in the range of $[1675, 1690][K]$. The isotherms are almost parallel lines in the crystal.

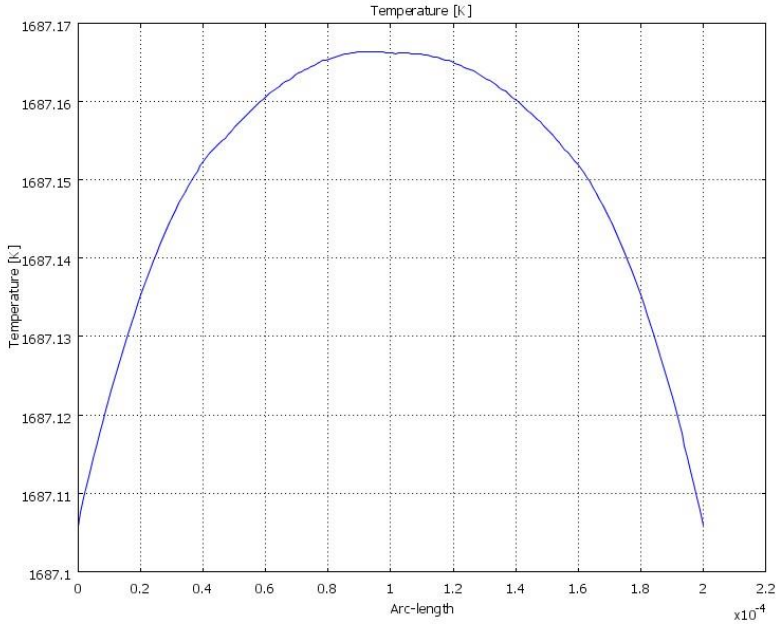

Figure13. Variation of the temperature field magnitude T across the meniscus, computed along the line defined by $y = 1.4011 \cdot 10^{-4}\,[m]$ = meniscus height

According to Fig. 13, the temperature field magnitude T varies along the meniscus height level in the range of $[1687.105, 1687.165][K]$.

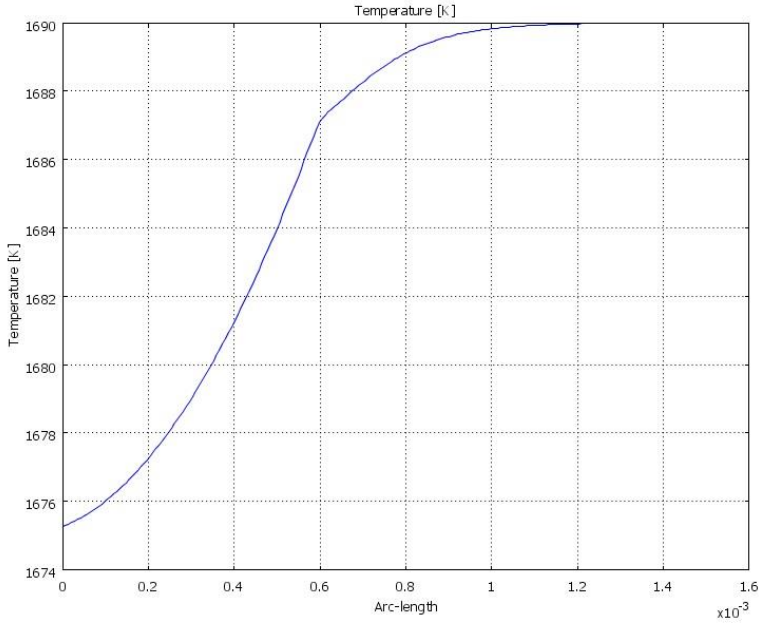

Figure 14. Variation of the temperature T along the sample, computed on the OY axis

According to Fig. 14, the temperature T varies in the range of $[1675, 1690][K]$ along the sample, computed on the OY axis.

3. IMPURITY DISTRIBUTION IN A TAPE GROWN BY PD GROWTH PROCESS

The quality of a monocrystalline sheet being grown by PD growth technique depends to a great extent on homogeneity of distribution of both specially added and detrimental impurities. Variations of concentrations of such impurities along the sheet length and cross-section are determined by the processes that take place in the melt near to the crystallization front. The impurity transport equation in the CO2 domain is that of the convection and diffusion equation which incorporates also the thermal diffusion:

$$\partial c/\partial t+\nabla\left(-D\nabla c\right)=R-(\vec{u}+\sigma D\nabla T)\nabla c \tag{4}$$

In this equation the following notations are used: c - impurity concentration; D - molecular diffusion; σ - Soret coefficient; R - reaction rate. At this point, it has to be mentioned that the term $\sigma Dc\Delta T$, which appears in the formula of the thermal diffusion contribution $\sigma D\nabla(c\cdot\nabla T)=\sigma D(\nabla c\cdot\nabla T+c\cdot\Delta T)$ is neglected in (4). This approximation is justified when the variation of T is nearly linear. For more details, see [5], [6] and [7]. It is also assumed, that there is no reaction in the melt, so $R=0$. The impurity concentration is subjected to the following boundary conditions: boundaries 1, 2, 3, 10, 11, 9 – insulation; boundary 4 – constant concentration; inner boundary 7 - impurity rejection according to the law: $v\cdot(1-k_0)\cdot c$, where v is the pulling rate and k_0 is the partition coefficient. For Al doped Si tape the following numerical data were used: $D=5.3\cdot10^{-8}[m^2/s]$; $\sigma=4.9\cdot10^{-4}[K^{-1}]$; $c_0=1\cdot10^{-2}[mol/m^3]=$Al concentration at boundary 4; inward flux due to rejection $=0.0001\cdot(1-2\cdot10^{-3})\cdot c[mol/(m^2\cdot s)]$ on the inner boundary 7; $k_0=2\cdot10^{-3}$. The impurity concentration is also subjected to the initial condition $c(t_0)=c_0$ constant. In Figs. 15-17, different details concerning the computed concentration field in the capillary channel and in the meniscus are presented.

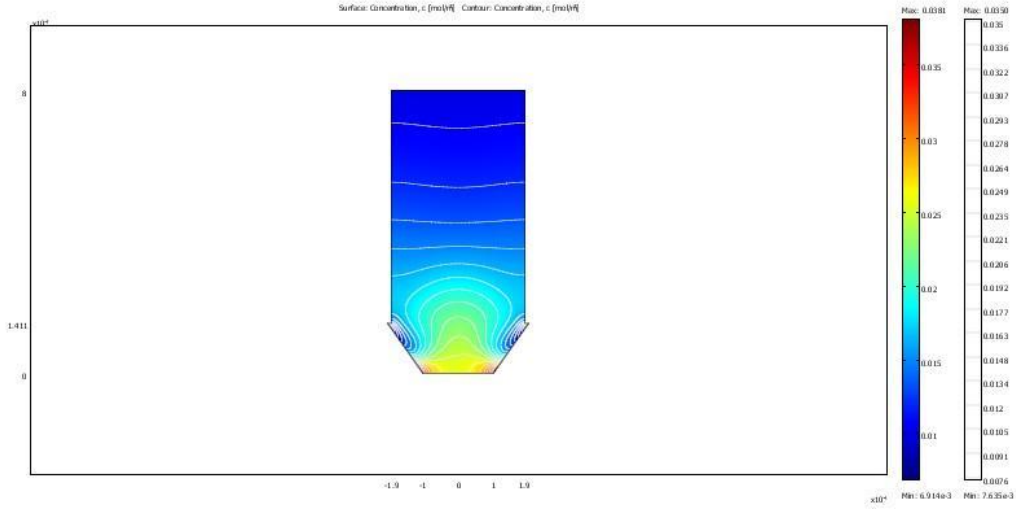

Figure 15. Dependence of the Al concentration c on the position, isoconcentration lines

According to Fig. 30, the Al concentration field magnitude c varies depending on the position in the range of $[0.01, 0.038][mol/m^3]$. The isoconcentration lines are almost parallel in the capillary channel but their form and disposal is much more complex in meniscus.

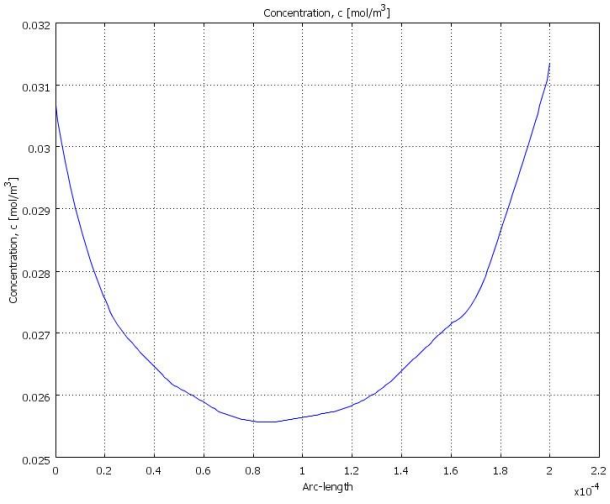

Figure 16. Variation of the Al concentration field magnitude c across the meniscus, computed along the line defined by $y = 2 \cdot 10^{-5}[m]$.

According to Fig. 16, the Al concentration across the meniscus close to the crystallization front varies in the range of $[0.0255, 0.031][mol/m^3]$. The concentration is minimal at the middle of the meniscus and is maximum at the margins of the meniscus. It follows that the Al concentration in the crystal side is $6.2 \cdot 10^{-5}[mol/m^3]$ at the margins and is $5 \cdot 10^{-5}[mol/m^3]$ at the middle. So, the impurity segregation coefficient across the plate is 1.24. The increase of concentration close to the crystallization front is due to the rejection of Al at the interface. The non-uniformity of concentration across the meniscus is due to the Marangoni flow. According to Fig. 17, the Al concentration along the capillary channel and meniscus, computed on the OY axis, increases from the top of the capillary channel to the bottom of the meniscus. This global increase is due to the rejection. In the capillary channel the Al concentration increases from $0.01[mol/m^3]$ (at the top) to $0.023[mol/m^3]$ (at the bottom) and in meniscus the Al concentration increases from $0.023[mol/m^3]$ (at the meniscus top) to $0.026[mol/m^3]$ (at the meniscus bottom).

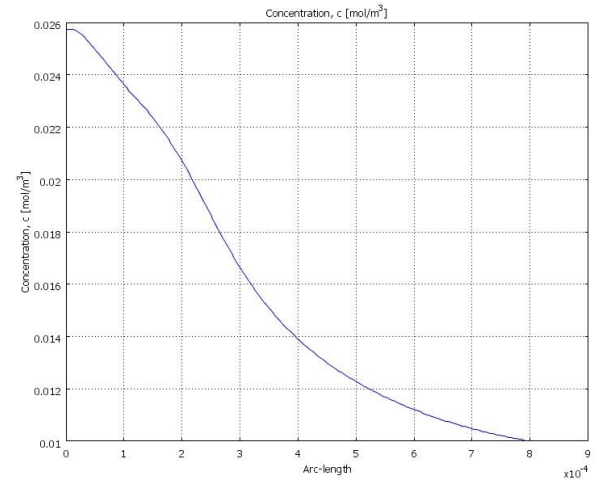

Figure17. Variation of the Al concentration along the meniscus and capillary channel computed on the OY axis

4. CONCLUSIONS

In the framework of the presented description, the following quantities, related to the micro tape growth process from the melt by pulling down method, can be computed:

- heat distribution in the melt-crystal system and the flow in the melt taking into account the volume force field including the buoyancy force field, pulling rate, thermal Marangoni flow, heat release due to the solidification and heat loose due to the cooling,
- added impurity distribution in the meniscus and capillary channel taking into account the molecular diffusion, thermal diffusion (i.e. Soret effect) and impurity rejection at the front of solidification,
- impurity segregation across the micro-plate which has been grown.

ACKNOWLEDGEMENT

This research did not receive any specific grant from funding agencies in the public, commercial, or not-for-profit sectors.

REFERENCES

[1] A. M. Balint, St. Balint, A 2D description of the single crystal thin plate growth from the melt by micro - pulling - down method. Part 1, *INCAS BULLETIN*, (online) ISSN 2247–4528, (print) ISSN 2066–8201, ISSN–L 2066–8201, (emerging in vol **10**, issue 3, 2018).

[2] W.-K. Rhim, K. Ohsaka, Thermophysical properties measurement of molten silicon by high-temperature electrostatic levitator: density, volume expansion, specific heat capacity, emissivity, surface tension and viscosity, *Journal of Crystal Growth*, Volume **208**, Issues 1–4, Pages 313-321, 1 January 2000.

[3] H. M. Ettouney, R. A. Brown, Analysis of operating limits in edge-defined film-fed crystal growth, *Journal of Crystal Growth*, Volume **62**, Issue 2, Pages 230-246, July 1983.

[4] K. A. Cliffe, S. J. Tavener, Marangoni–Bénard Convection with a Deformable Free Surface, *Journal of Computational Physics*, Volume **145**, Issue 1, Pages 193-227, 1 September 1998.

[5]. D. J. Larson Jr. and B. S. Dressler, Shuttle mission 51-G, experiment MRS77F075 Flight sample characterization report, *NASA Report, Re-753*, 1988.

[6]. L. L. Zheng, D. J. Larson Jr. and H. Zhang, Role of thermotransport (Soret effect) in macrosegregation during eutectic/off-eutectic directional solidification, *Journal of Crystal Growth*, Volume **191**, Issues 1–2, Pages 243-251, 1 July 1998.

[7]. E. Tulcan-Paulescu, A. M. Balint and St. Balint, The effect of the initial dopant distribution in the melt on the axial compositional uniformity of a thin doped crystal grown in strictly zero-gravity environment by Bridgman–Stockbarger method, *Journal of Crystal Growth*, Volume **247**, Issues 3–4, Pages 313-319, January 2003.